

## Hot Corrosion Behavior of FeAl Intermetallic Compound Modified with Ti, and Cr in Molten Salt Mixture KCl-ZnCl<sub>2</sub>

R. A. Rodríguez-Díaz<sup>1,\*</sup>, J. Uruchurtu-chavarín<sup>1</sup>, J. Porcayo-Calderon<sup>1</sup>, J. M. López-Oglesby<sup>2</sup>, M. E. Mendoza<sup>3</sup>, J. J. Ramos-Hernández<sup>4</sup>, S. Valdez<sup>5</sup>, A. Bedolla<sup>6</sup>.

<sup>1</sup> Centro de Investigación en Ingeniería y Ciencias Aplicadas, UAEM, Av. Universidad 1001, Col. Chamilpa, Cuernavaca Mor., México.

<sup>2</sup> Universidad Popular Autónoma del Estado de Puebla, A. C.; 21 sur No. 1103, Colonia Santiago, C. P. 72160 Puebla, Puebla, México.

<sup>3</sup> Instituto de Física, Universidad Autónoma de Puebla, Apartado Postal J-48, Puebla 72570, México.

<sup>4</sup> I.I.E., Gerencia de Procesos Térmicos, Av. Reforma 120, Temixco, Mor., México.

<sup>5</sup> Instituto de Ciencias Físicas-UNAM, Av. Universidad S/N, Col. Chamilpa, Cuernavaca, C.P. 62210, Morelos, México

<sup>6</sup> Instituto de Investigaciones Metalúrgicas, UMSNH. Edificio "U", Ciudad Universitaria, 58066 - Morelia, Michoacán, México.

\*E-mail: [rdiaz.unam@gmail.com](mailto:rdiaz.unam@gmail.com)

Received: 31 January 2013 / Accepted: 3 March 2013 / Published: 1 May 2013

---

The hot corrosion behavior of Fe<sub>40</sub>Al intermetallic alloyed with 2.5 at. % Cr and Ti in KCl-ZnCl<sub>2</sub> (1:1M) at 450°C has been evaluated by using electrochemical techniques. Techniques included potentiodynamic polarization curves, linear polarization resistance (LPR) and electrochemical impedance spectroscopy (EIS) measurements. Furthermore thermodynamic stability phase diagrams were calculated and elaborated in order to describe the corrosion process. Results have shown that additions of both Cr and Ti increased the corrosion rate, besides the alloy was passivated by adding Cr. Addition of Ti induced a better corrosion performance than Fe<sub>40</sub>Al<sub>2.5</sub>Cr alloy, this behavior is due to the formation of a non-porous aluminum oxide layer modified with titanium oxide. Corrosion behavior is explained in terms of the stability of the corrosion products formed film.

---

**Keywords:** Hot corrosion, Fe<sub>40</sub>Al intermetallic, electrochemical techniques.

### 1. INTRODUCTION

Incineration is one of the most widely used alternatives for the management of municipal solid waste [1]. Incineration has a lower environmental impact than other alternatives such as dumping and

the energy generated by the combustion process is transformed into electric energy via a system steam turbine [2]. However, efficient operation of waste combustion plants is hampered by the occurrence of severe corrosion problems. The gases produced during combustion processes are drawn into the heat exchanger zone where produce steam. These gases contain ash from the combustion process. The impact and adhesion in the exchanger tubes are responsible for the corrosion produced as a result of surface degradation and erosion processes [3].

Detailed studies of this ash have demonstrated that one of the most important corrosive agents are salts that form chlorinated mixtures of low melting points [4]. One of the most aggressive corrosive compounds found in the ashes collected from incinerators is the eutectic mixture of chloride salts KCl: ZnCl<sub>2</sub> [5, 6]. This mixture and other compounds, such as NaCl and K<sub>2</sub>SO<sub>4</sub> cause damage to pipes through the inertial transport mechanism. This process includes both the impact and the adhesion of melted salts, producing both erosion and corrosion processes [3]. The corrosion and erosion generating ash originating in these incinerators requires testing for thickness changes in the exchanger tubes to identify damaged and out-of-spec tubes that may fail and potentially cause dangerous situations and heavy, expensive and/or time-consuming losses.

In order to reduce the failure rate of superheater components, it is necessary to develop more effective protective coatings for such components operating in hostile combustion environments. Normally, Ni-based alloys suffer less corrosion by chlorine but they are susceptible to accelerated corrosion in environments of high sulfur activity [7], leading to catastrophic liquid phase corrosion. In addition, Ni-based alloys are relatively expensive.

Al-bearing alloys represent good candidate coating materials for such environments, considering the reduced costs and useful properties such as low density, high strength and good wear resistance [8, 9]. It is known that Fe–Al alloys with contents greater than 10 wt% Al possess good oxidation–sulphidation resistance [10]. Fe–Al alloys also exhibit much better corrosion resistance than Cr-based coatings in Cl- or Cl–S-environments, especially at temperatures above 600°C [11-13].

To get more information about the mechanisms of corrosion that occur in these exchangers, electrochemical techniques are more appropriate than gravimetric methods [14-17].

Since the molten salts act as electrolytes, electrochemical techniques such as potentiodynamic polarization curves can be utilized [14]. Sequeira and Honking [15] studied the corrosion behavior of Ni in molten Na<sub>2</sub>SO<sub>4</sub>, NaCl, and in mixtures of these two salts, at 900° C, in laboratory air and under O<sub>2</sub>+SO<sub>2</sub>/SO<sub>3</sub> atmospheres. The authors inferred from polarization curves that Ni in pure NaCl showed the lack of a passive region; and the occurrence of extensive intergranular attack.

Espinosa-Medina et al., [16] evaluated the hot corrosion resistance of sprayed and atomized Fe–40 at.% Al, Fe40Al+0.1B and Fe40Al+0.1B+10Al<sub>2</sub>O<sub>3</sub> intermetallic materials in NaVO<sub>3</sub> at 625 and 700°C using polarization curves and LPR measurements during 10 days of exposure. The authors related corrosion rates with the establishment of an Al<sub>2</sub>O<sub>3</sub> layer, which is more protective in Fe40Al+0.1B+10Al<sub>2</sub>O<sub>3</sub> alloy and also increased its protectiveness as the temperature increased.

Pan et al., [17] studied the corrosion resistance of 12CrMoV steel exposed to a molten mixture of (55–45) mol.% ZnCl<sub>2</sub>–KCl in air at 400 °C by Electrochemical Impedance Spectroscopy (EIS). The authors reported that initial Nyquist plots of 12CrMoV exhibited a semicircle at high frequencies and a line at low frequencies related to a diffusion-controlled reaction. Zeng et al., [18] studied the corrosion

behavior of Ni and FeAl in molten  $(0.62\text{Li}, 0.38\text{K})_2\text{CO}_3$  mixtures in air at  $650^\circ\text{C}$  by EIS. The Nyquist curves for Ni showed the typical characteristics of a diffusion-controlled reaction, a semicircle at the high-frequency and a line at the low-frequency port. The corrosion behavior of FeAl also exhibited the feature of a diffusion-controlled reaction during initial immersion. However, the impedance spectra were composed of two capacitance loops after some immersion time. The authors found that change of the Nyquist curves with immersion time could be related to the formation of continuous external  $\text{LiFeO}_2$  and an inner  $\text{Al}_2\text{O}_3$  layer.

This work deals with an electrochemical study of the effect of adding 2.5 at.% Cr and Ti to a Fe40Al intermetallic alloy exposed to a corrosive salt mixture composed of  $\text{KCl-ZnCl}_2$  (1:1M) at  $450^\circ\text{C}$ . The aim of present investigation is to suggest a potential improvement for incinerator heat exchanger linings that will better tolerate the extreme conditions of heat and abrasion experienced by these components.

## 2. EXPERIMENTAL PROCEDURE

### 2.1 Materials

Cast ingots of binary Fe-40 at. % Al and ternary Fe40Al-X (X = 2.5 at. % Cr, Ti) alloys were fabricated using a high-frequency induction furnace at approximately  $1500^\circ\text{C}$ . High purity (99.9 %) Fe, Al, Cr and Ti were placed in a silicon carbide crucible for induction melting. The molten Fe-40Al and Fe40Al-X alloys were poured into a rectangular copper mold and subsequently solidified during cooling until room temperature was reached, obtaining in this way a coarse grain microstructure.

### 2.2 Sample preparation

The produced ingots were cut by a diamond wheel cutter into small rectangular parallelepiped pieces of surface area ranging from 1.5 to  $2.5\text{cm}^2$ . The electrical contact was made by welding a Ni20Cr wire to the specimen. Once welded to the specimen, the wire was put inside an alumina tube (2 mm inner diameter), so that the specimen remained at one end of the tube, where it was sealed with a refractory cement. The experimental apparatus used in the present study is very similar to that employed in a previous research [19].

### 2.3 Electrochemical techniques

Electrochemical techniques for characterizing the corrosion at high temperature included potentiodynamic polarization curves, linear polarization (LPR) and EIS measurements. The body of the test cell was a 25 ml alumina crucible.

The most important elements were a reference and auxiliary electrodes, made of a 0.5 mm diameter (Pt) wire inside a mullite tube and filled with ceramic cement. The amount of salt in each run

was 0.5 g for an exposed area of 1.0 cm<sup>2</sup> under static conditions, without stirring the molten salt. The electrical contact was made by welding an 80 wt.% Cr–20 Ni wire to the specimen.

Polarization curves were obtained by polarizing the specimens from -500 to +1000 mV<sub>Pt</sub> with respect to the free corrosion potential value,  $E_{corr}$ , at a scanning rate of 1.0 mV/s. Corrosion current density values,  $I_{corr}$ , were calculated by using the Tafel extrapolation method taking an extrapolation zone of  $\pm 250$  mV around the  $E_{corr}$  value.

LPR measurements were carried out by polarizing the specimen from -10 to +10 mV with respect to  $E_{corr}$ , at a scanning rate of 1 mV/s, repeated every 20 minutes over a period of 24 hours. EIS measurements were done in the frequency interval of 0.05 to 30000 Hz at the  $E_{corr}$  value by using a PC4-300 Gamry potentiostat. The amplitude of the input sine-wave voltage was 10 mV.

Three measurements were performed in each case. The working salt consisted of 500 mg/cm<sup>2</sup> of an eutectic mixture of KCl-ZnCl<sub>2</sub> (1:1 M analytical grade) for each test. The testing temperature was 450°C in static air condition. Prior to the tests, the specimens surfaces were prepared by the standard technique of grinding with SiC from 240 to 600 grit emery paper, washed with water and degreased with acetone.

#### 2.4 Metallographic preparation and microstructural characterization of corroded specimens.

Some specimens taken after the LPR measurements were mounted in bakelite. Metallographic preparation of encapsulated specimens was performed by grinding the specimens with 240 to 1500 grit paper and polished with 1  $\mu$ m alumina slurry. The corroded specimen surfaces were analyzed with a scanning electron microscope (SEM) with an accelerating voltage of 25 keV. Chemical microanalysis was carried out with an energy dispersive X-ray analyzer (EDX) attached to the SEM.

### 3. RESULTS AND DISCUSSION

#### 3.1. Microstructural characterization of un-corroded alloys.

##### 3.1.1 Microstructure characterization by Scanning Electron Microscopy.

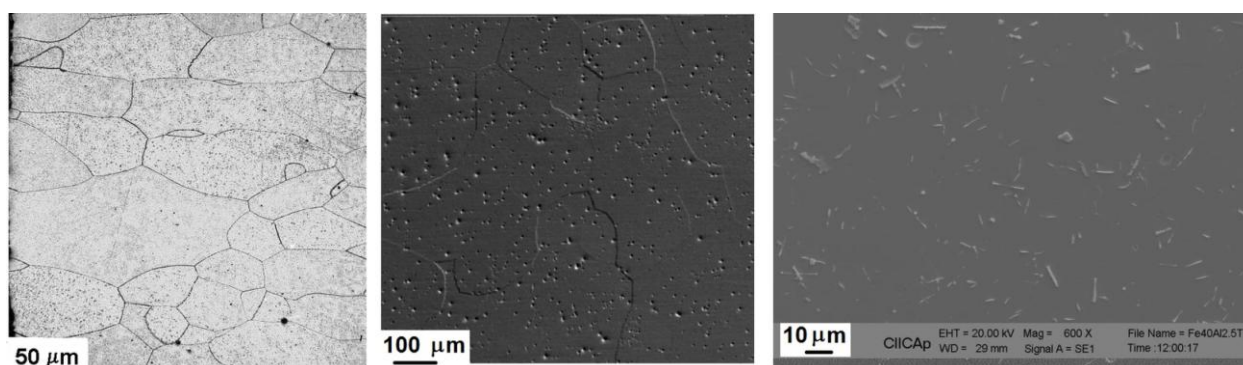


**Figure 1** Microstructures of the as-cast alloys a) Fe40Al b) Fe40Al2.5Cr and c) Fe40Al2.5Ti.

The microstructure of the as-cast Fe40Al alloy is shown in Figure 1 a), exhibiting grains with a predominantly columnar morphology. XRD, SEM and chemical analyses using the EDS technique did not reveal the presence of precipitates on the surface of this alloy. This observation is consistent with the wide interval of composition (35-50 at.% Al) which contains a FeAl phase with a B2-type crystal structure according to the phase diagram for the Fe-Al system [20]. This alloy presented a chill-type microstructure with three typical grain morphologies: chill, equiaxed and columnar. The mean size of chill morphology grains was  $276 \pm 88 \mu\text{m}$ , the dimensions of the columnar grains were  $280 \pm 94 \mu\text{m}$  in width and  $2200 \pm 130 \mu\text{m}$  in length and the size of equiaxed morphology grains was  $548 \pm 91 \mu\text{m}$ .

Figure 1 b) shows the microstructure of the as-cast Fe40Al2.5Cr alloy, which exhibited a predominantly equiaxed grain morphology with an average size of  $141.2 \pm 29.3 \mu\text{m}$ . EDS chemical analyses performed on Fe40Al2.5Cr alloy together with SEM observations did not reveal the existence of precipitates, which could have formed by the addition of Cr. According to the XRD profiles shown in Figure 2 b), this alloy presented a B2 crystal structure corresponding to the FeAl alloy without the presence of second phases. These results are consistent with Li et al., [21] who reported that the Cr element enters in solid solution in the FeAl matrix as long as the addition of this element does not exceed 5 at. %.

Figure 1 c) shows the as-cast Fe40Al2.5Ti alloy, which shows white precipitates with a predominantly acicular morphology uniformly distributed in the FeAl matrix. Microstructures of this alloy exhibit equiaxial grains with a mean size of  $150 \pm 10 \mu\text{m}$ . The EDS chemical analyses revealed that these precipitates were composed of Fe, Al and Ti, and correspond to a Fe2TiAl phase with a L21 Heusler-type crystalline structure. This is because the region which contains the Fe2TiAl phase is just above the zone in which exists the B2-type phase in the ternary Fe-Al-Ti phase diagram [22].

### 3.1.2. Microstructural characterization of un-corroded alloys by X-Ray Diffraction (XRD).

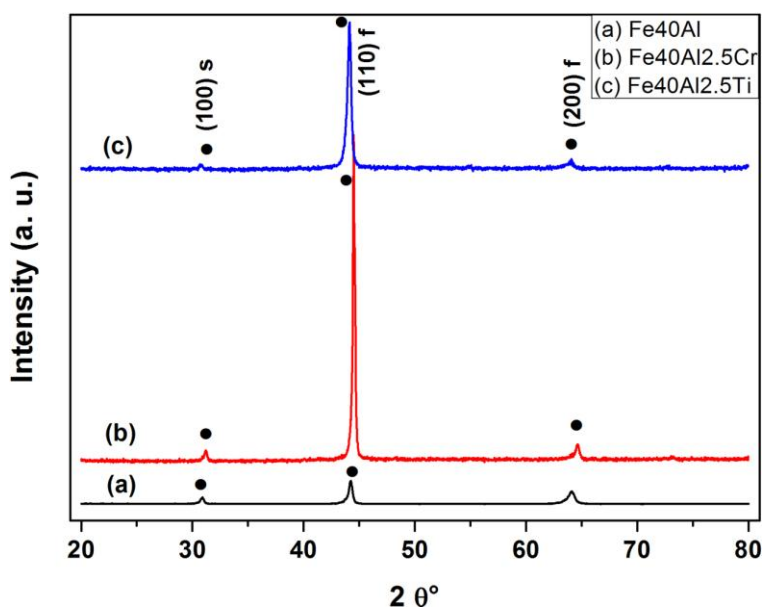


**Figure 2.** X-Ray diffraction patterns of the as-cast alloys a) Fe40Al b) Fe40Al2.5Cr and c) Fe40Al2.5Ti.

Figure 2 shows the XRD patterns of as-cast Fe40Al, Fe40Al2.5Cr and Fe40Al2.5Ti (at. %) alloys, where fundamental (f) and super lattice peaks (s) corresponding to a cubic B2-type ordered crystal structure are shown. The presence of these peaks indicates that Cr and Ti do not modify the B2 ordered crystalline structure. Additional peaks pertaining to second phases or precipitates were not detected in Figures 2 b) and c), suggesting that Cr entered in solid solution in the intermetallic B2 matrix as evidenced also by the absence of precipitates in micrograph showed in Figure 1 b). The absence of XRD diffraction peaks in Figure 2 b) pertaining to a Fe2TiAl phase with a L21 Heusler-type crystal structure observed in Figure 1 c) is related to the small size and concentration of these precipitates uniformly distributed in the FeAl-B2 matrix.

XRD analyses together with the scan line chemical analyses confirmed the total solubility of 2.5 at.% Cr in the FeAl-B2 matrix. These results are supported by Argawal et al., [23-24], who found that Cr additions were completely dissolved in a Fe<sub>3</sub>Al intermetallic matrix, without forming second phases or precipitates.

Figures 2 a), b) and c) do not exhibit all diffraction peaks, which is related to a large grain size and a preferred surface crystallographic orientation on samples.

### 3.2 Potentiodynamic polarization curves.

Polarization curves for binary Fe40Al and ternary Fe40Al2.5Cr, Fe40Al2.5Ti alloys are displayed in Figure 3. This figure shows an active behavior only for the binary Fe40Al intermetallic alloy, with an  $E_{corr}$  value close to -330 mV and a corrosion rate, expressed in terms of the  $I_{corr}$  value, close to 0.3 mA/cm<sup>2</sup>. In a previous investigation, Porcayo et al., [25] reported a value of the corrosion potential  $E_{corr}$  equal to -141 mV with an  $I_{corr}$  value of 1.89 mA/cm<sup>2</sup> in a 304 SS sample that was corroded in the same salt mixture (KCl-ZnCl<sub>2</sub>) at 450 °C. Therefore, Fe40Al alloys exhibit a more active corrosion potential but a lower corrosion rate than 304 SS under these test conditions.

The anodic current density of binary Fe40Al alloy increased with increasing potential, but at around 90 mV a kind of anodic limiting current density was reached. This behavior may be due to the formation of a layer of corrosion products composed of a mixture of aluminum and iron oxides together with non-volatile metallic chlorides (see Figure 7 b), c), d), e) and f)). The existence of these compounds can be confirmed by looking at the thermodynamic stability diagram for Fe-Al-Cl-O system at 450°C shown in Figure 10.

With the addition of Ti  $E_{corr}$  became nobler, reaching a value of 156 mV, but became more active (more negative) with the addition of Cr (-975 mV). However, Fe40Al2.5Ti alloy presented a lower current density (0.4 mA/cm<sup>2</sup>) than Fe40Al2.5Cr alloy (0.8 mA/cm<sup>2</sup>), which means that addition of Ti induced a lower corrosion rate compared with the ternary Fe40Al2.5Cr alloy. Porcayo et al., [25] reported a current density value  $I_{corr}$  of 3.6 mA/cm<sup>2</sup> in a Ni20Cr wt % coating deposited on 304 stainless steel that was corroded in the same salt mixture (KCl-ZnCl<sub>2</sub>) at 450 °C. Therefore, all binary and ternary alloys studied in present work exhibited a lower corrosion rate (expressed in terms of current density) than Ni20Cr wt% coating deposited on 304 SS corroded under the same conditions [25].

Similarly, the corrosion current density value was increased after the addition of Cr and Ti. On the other hand, a passive region was found with Cr at a passivating potential value,  $E_{pas}$ , of -562 mV, reaching a passive current density,  $I_{pas}$ , close to 35 mA/cm<sup>2</sup>. This behavior is due to the formation of protective layer of Cr<sub>2</sub>O<sub>3</sub> besides de aluminum oxide scale. See Figures 8 d) and e), where chemical mappings of Cr and O are shown respectively. Table 1 summarizes all these parameters.

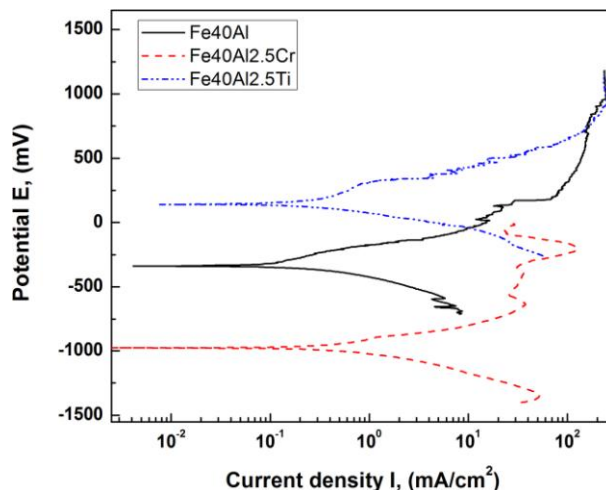


**Figure 3.** Polarization curves for binary Fe40Al and ternary Fe40Al2.5Cr and Fe40Al2.5Ti alloys in the KCl+ZnCl<sub>2</sub> mixture at 450°C.

**Table 1.** Electrochemical parameters obtained from the polarization curves.

Alloy	$E_{corr}$ (mV)	$I_{corr}$ (mA/cm <sup>2</sup> )	$E_{pas}$ (mV)	$I_{pas}$ (mA/cm <sup>2</sup> )	$E_{pit}$ (mV)
Fe-40Al	-330	0.3	---	---	---
Fe-40Al-2.5Cr	-975	0.8	-562	50	-337
Fe-40Al-2.5Ti	156	0.4	---	----	----

### 3.3 LPR measurements.

The change in the linear polarization resistance value with time,  $R_p$ , for the different alloys in the KCl+ZnCl<sub>2</sub> mixture is shown in Figure 4. When alloying with either Ti or Cr, the  $R_p$  value increased (various orders of magnitude in the case of Cr), and thus exhibited a decrease in the corrosion rate. This could be due to the formation of an Al<sub>2</sub>O<sub>3</sub> layer, modified with Cr<sub>2</sub>O<sub>3</sub>, TiO<sub>2</sub>, Ti<sub>2</sub>O<sub>3</sub> or TiO. The existence of aluminum oxide scale is explained by looking at the thermodynamic stability diagram for Fe-Al-Cl-O system at 450°C shown in Figure 10, where the Al<sub>2</sub>O<sub>3</sub> phase is stable in a wide region of chlorine and oxygen ( $P_{cl}$  and  $P_{O_2}$ ) partial pressures. Similarly, the formation of chromium oxide and titanium oxides scales is corroborated by looking at the thermodynamic stability diagrams for Fe-Al-Cr-Cl-O and Fe-Al-Ti-Cl-O systems at 450°C presented in Figures 11 (a) and (b), where the Cr<sub>2</sub>O<sub>3</sub>, TiO<sub>2</sub>, Ti<sub>2</sub>O<sub>3</sub> or TiO are the main stable phases in a wide region of chlorine and oxygen ( $P_{cl}$  and  $P_{O_2}$ ) partial pressures. However, the Cr<sub>2</sub>O<sub>3</sub> phase is stable over a narrower region than Al<sub>2</sub>O<sub>3</sub>.

It is important to note that titanium oxide phases ( $Ti_xO_y$ ) are stable in a region extension slightly minor than the zone in which  $Al_2O_3$  is stable.

The  $R_p$  value of the ternary Fe40Al2.5Cr alloy exhibited a more erratic variation as compared to unalloyed FeAl and ternary Fe40Al2.5Ti alloys as the immersion time elapsed. This behavior can be associated with the passivation-repassivation processes. In addition, this tendency can be explained in terms of the stability of the external corrosion products layer: if this layer is very stable, and it is not detached from the metal surface, the  $R_p$  value remains more or less constant; but if this layer is detached and formed again, the  $R_p$  value will fluctuate with time [14]. Thus, in this case Fe40Al and Fe40Al2.5Ti exhibited a more stable layer of corrosion products compared with ternary Fe40Al2.5Cr alloy.

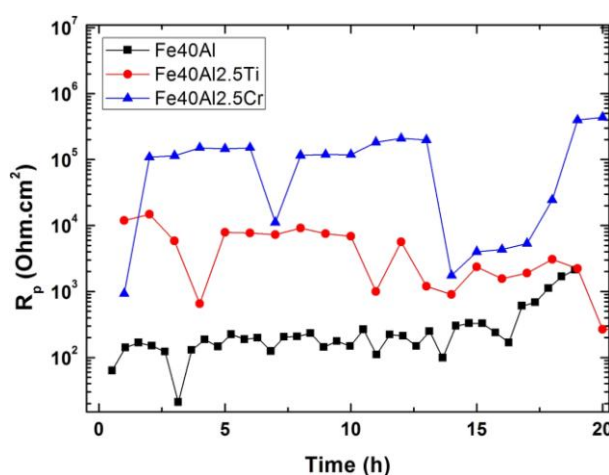


**Figure 4.** Change in the  $R_p$  value with time for binary Fe40Al and ternary Fe40Al2.5Cr or Fe40Al2.5Ti alloys in the KCl+ZnCl<sub>2</sub> mixture at 450°C.

### 3.4. EIS measurements.

Nyquist diagrams for binary Fe40Al intermetallic alloy exposed to the KCl+ZnCl<sub>2</sub> mixture at 450 °C are shown in Figure 5. For immersion times under 5 hours, the data describe a single capacitive-like semicircle, with its center on the real axis and its diameter increasing with time. This diagram indicates that the corrosion process is under charge transfer from the metal to the electrolyte through the double electrochemical layer. For times greater than 5 hours, in addition to the high-frequency capacitive semicircle there is an uncompleted low-frequency semicircle. The diameter of the low-frequency semicircle is much bigger than that for the high-frequency semicircle and it has a trend to decrease as time elapses. The emergence of a large capacitive loop at the low-frequency region may indicate the formation of a protective scale on the alloy surface which is in agreement with polarization curve of Fe40Al alloy shown in Figure 3, where a kind of anodic limiting current density was reached at around 90 mV. This behavior can be due to the formation of a layer of corrosion products composed mainly by a mixture of Al and Fe protective oxides and other compounds such as metals chlorides, see Figure 7 b), c), d), e) and f).

For the ternary Fe40Al2.5Cr alloy (Figure 6), the data describe, at all exposure times, a semicircle at high and intermediate frequency values followed by a second semicircle at low frequency values, with its diameter increasing with time. This time, the high-frequency semicircle diameter is lower than that for unalloyed Fe40Al alloy (Figure 5). A similar behavior of Nyquist curves was observed for the alloy with the addition of Ti (Figure 7). However, the low-frequency semicircle diameter this time shows an erratic behavior, since sometimes it increases with time, and some other times it decreases. This may be due to the disruption of the external layer formed by the corrosion products or to the dissolution of any protective oxide layer formed on top of the alloy, which is dissolved by the molten salt.

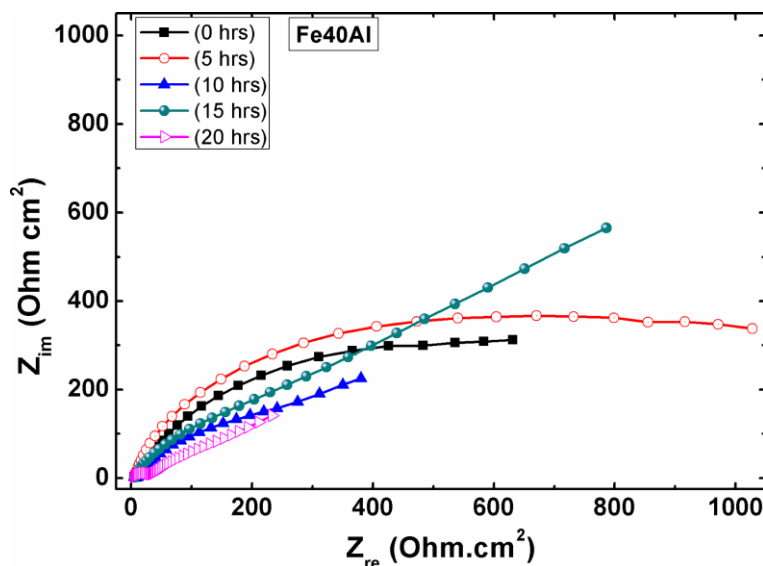


Figure 5 Nyquist diagrams for Fe40Al in the KCl+ZnCl<sub>2</sub> mixture at 450°C.

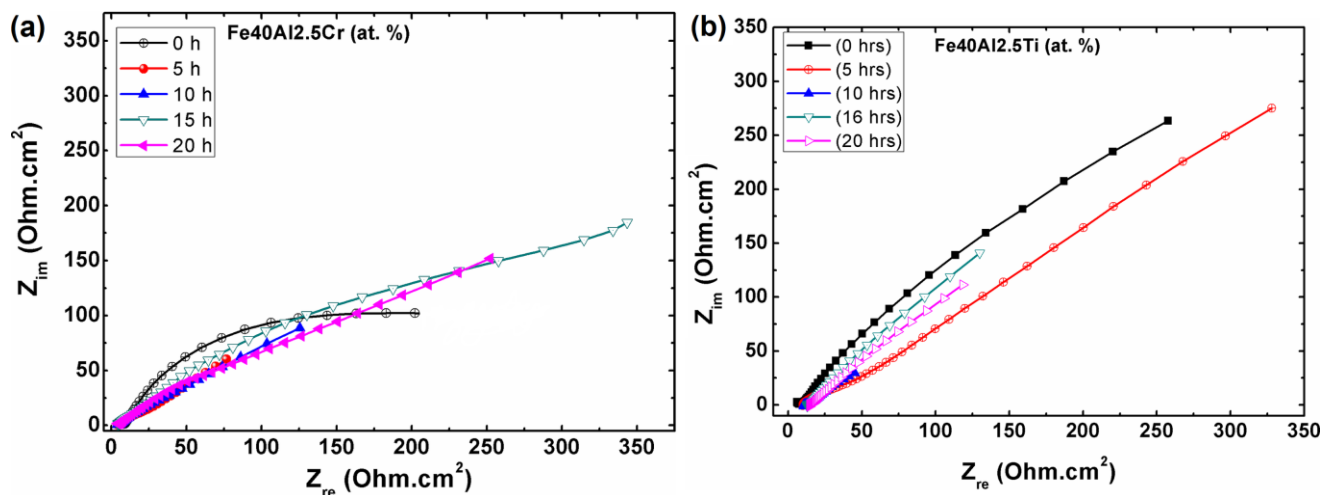


Figure 6. Nyquist diagrams for (a) Fe40Al2.5Ti and (b) Fe40Al2.5Cr in the KCl+ZnCl<sub>2</sub> mixture at 450°C.

### 3.5. Microstructural characterization of corroded alloys.

Some regions of corroded specimens after the LPR measurements were analyzed with a scanning electronic microscope (SEM). Figure 7 shows a micrograph of corroded Fe40Al base alloy together with the corresponding X-ray mappings of Fe, Al, Cl, O and Zn. The presence of O and Al on the external layer, although the Al-layer is discontinuous, led us to infer that there was some Al<sub>2</sub>O<sub>3</sub> layer formed on top surface of the alloy. In addition to this, there was Cl present below the Al<sub>2</sub>O<sub>3</sub> superficial layer, which indicates that the molten salt had dissolved the iron oxide scale and permeated through it. This rapidly degraded the oxide's protective properties, leading to a continuous degradation of the alloy. The melting point of the ZnCl<sub>2</sub>-KCl salt mixture used for the tests was only of about 250 °C, so that it was molten at the experimental operation temperature, making the establishment of protective scales over these Fe-Al based alloys more difficult.

The dealloying or demetallification of Al shown in Figure 7 b) was due to the diffusion of Cl<sub>2</sub> through cracks and pores of the scale down to the alloy/scale interface, where it reacted with the metallic alloy to form the volatile AlCl<sub>3</sub> compound, in accordance to the reaction shown in Equation 1:



Since the boiling point of AlCl<sub>3</sub> is approximately 178 °C [26], the metal chloride diffused out of the scale, resulting in a lack of Al under the protective aluminum oxide layer.

The presence of Fe and Cl shown in Figures 7 c) and e) may indicate the presence of FeCl<sub>2</sub> that could be formed according to the reaction shown in Equation 2:



The presence of Fe contained in iron chloride compounds, which is seen in the X-ray mapping in Figure 7 c) was due to the high melting and boiling points of FeCl<sub>2</sub> with values of 677 and 1023 °C, respectively [26].

Similar characteristics were exhibited by the ternary Fe40Al2.5Cr alloy (Figure 8) where the presence of an Al-containing oxide on the top external surface which was dissolved by chloride ions was observed. Similarly, the dealloying of Al and the presence of Fe in Figures 8 b) and c) can also be attributed to the formation of AlCl<sub>3</sub> and FeCl<sub>2</sub> as explained in preceding paragraphs.

At vapor pressures higher than 10<sup>-4</sup> atm. [27], the metal chlorides diffuse out of the metal/oxide interface and are transformed into Fe<sub>2</sub>O<sub>3</sub>, Al<sub>2</sub>O<sub>3</sub> and Cr<sub>2</sub>O<sub>3</sub> precipitates at sites of sufficiently large oxygen pressure within the scale according to the reactions 20, 8 and 7 included in Table 2. The presence of Fe and O in X-ray mapping shown in Figures 7 c), 7 d), 8 b) and 8 e) indicates the formation of iron oxide according to the reaction 20 included in Table 2.

Similarly, the presence of Cr and O in Figures 8 d) and e) denotes the formation of protective Cr<sub>2</sub>O<sub>3</sub> compound according to the reaction 8 included in Table 2.

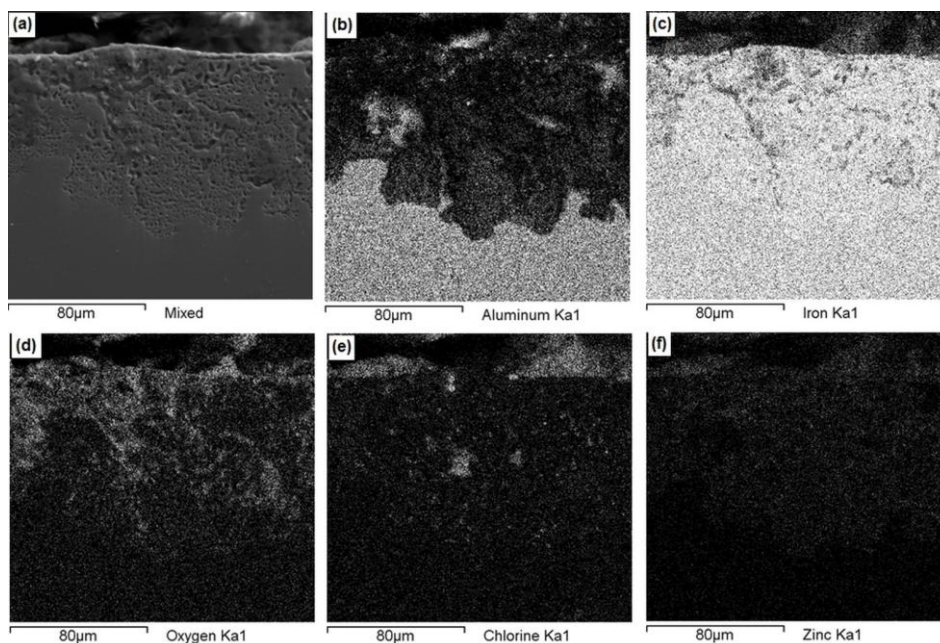


**Figure 7.** Photomicrographs of (a) Fe40Al corroded in the KCl+ZnCl<sub>2</sub> mixture at 450°C together with X-ray mappings of (b) Al, (c) Fe, (d) O, (e) Cl and (f) Zn.

In similar way, Figure 9 shows micrographs of corroded Fe40Al2.5Ti alloy together with the corresponding X-ray mappings of Al, Cl, O and Ti. Figures 9 b) and e) suggest the existence of a continuous protective layer of aluminum oxide modified with titanium oxide which improves its protectiveness. The presence of Cl in the external oxide protective scale can be explained as follows: most of the chloride ions did not diffuse to the interior of metallic alloy through the interface metal/oxide. Rather, Cl ions reacted with Al and Ti contained in protective oxide top external layer, leading to the formation of iron and/or titanium chlorides according to the reactions 23 and 29 included in Table 2.

Although the top surface aluminum oxide layer present in the Cr-containing alloy seems to be more porous than that present in the Ti-containing alloy (see Figure 9) this may be the reason why the latter was more corrosion resistant than the former according to polarization curves shown in Figure 3 and the electrochemical parameters obtained from polarization curves in Table 1. Furthermore, Li et al. [28] studied the influence of Ti addition on the high temperature oxidation behavior of FeAl intermetallic alloys in air at 1000°C and 1100°C. The authors established that 2 at. % Ti addition can enhance the oxidation resistance of Fe-36.5Al alloy because of the formation of a protective TiO layer in the surface. Therefore, the higher corrosion resistance exhibited by FeAl2.5Ti alloy as compared with that of FeAl2.5Cr, as likely due to the continuous character of aluminum oxide layer together with the beneficial protective effect induced by TiO formation in Al<sub>2</sub>O<sub>3</sub> scale.

The detrimental effect of Cr observed in present work is in agreement with previous investigations. A deleterious effect of the presence of Cr on the corrosion resistance of several commercial steels in oxygen induced by a ZnCl<sub>2</sub>- KCl molten mixture has been reported by Li et al., [29]. In the same manner, Shinata et al. [30] stated that increasing the chromium content of stainless

steels under NaCl deposits did not improve their corrosion resistance. Even pure Cr showed a fast corrosion rate in O<sub>2</sub> atmosphere under deposits of KCl [31] or of a KCl–ZnCl<sub>2</sub> molten mixture [32]. In the last two cases the high corrosion rate of Cr was associated to the formation of metal chromates soluble in the melt.

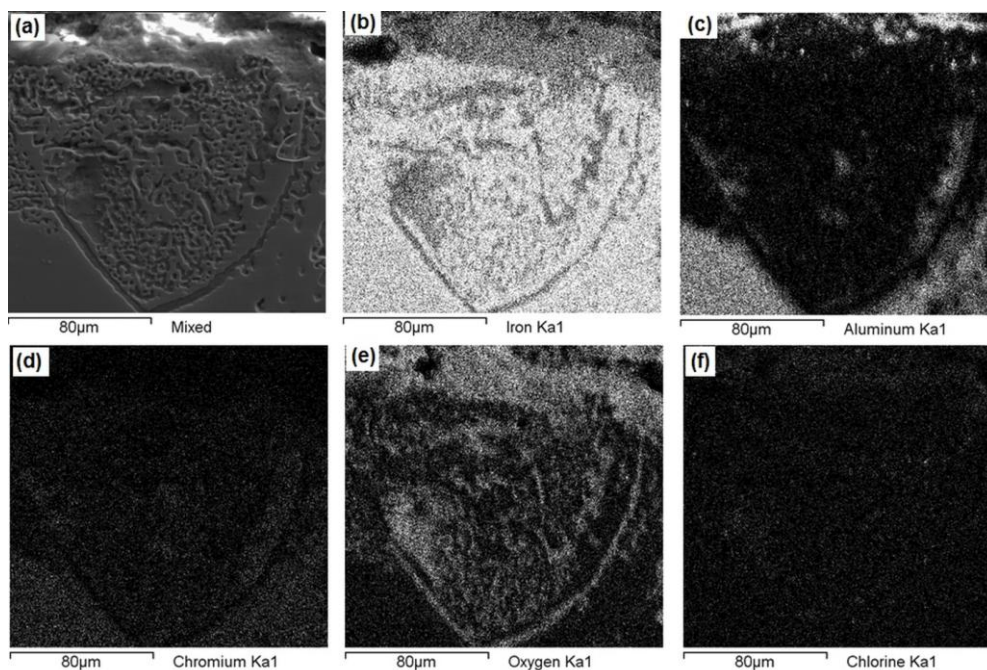


**Figure 8.** Photomicrographs of (a) Fe<sub>40</sub>Al<sub>2.5</sub>Cr corroded in the KCl+ZnCl<sub>2</sub> mixture at 450°C together with X-ray mappings of (b) Fe, (c) Al, (d) Cr, (e) O and (f) Cl.

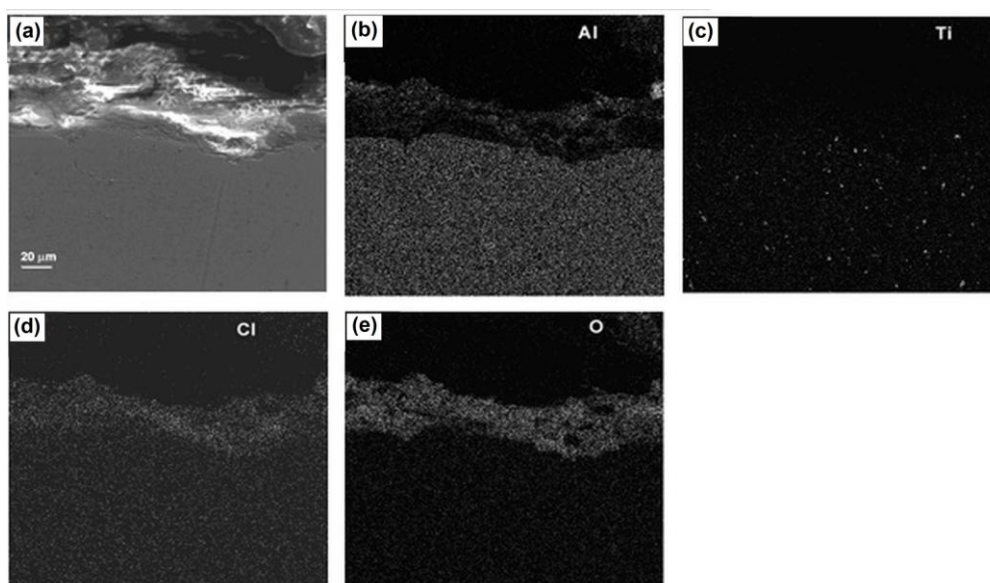


**Figure 9.** Photomicrographs of (a) Fe<sub>40</sub>Al<sub>2.5</sub>Ti corroded in the KCl+ZnCl<sub>2</sub> mixture at 450°C together with X-ray mappings of (b) Al, (c) Ti, (d) Cl and (e) O.

### 3.6 Phase-stability thermodynamic analysis.

Superimposed phase stability diagrams for the metal-chlorine-oxygen (M-Cl-O) systems, where M corresponds to Fe, Al, Cr or Ti taken at unit activity, were elaborated for a temperature of 450 °C to anticipate the possible corrosion products and also to provide a more appropriate understanding of the corrosion mechanism. The phase stability diagrams were constructed from equilibrium constants of chemical reactions included in Table 2. Figures 10, 11 (a) and (b) show the thermodynamic stability diagrams for Fe-Al-Cl-O, Fe-Al-Cr-Cl-O and Fe-Al-Ti-Cl-O at 450 °C respectively. The overall agreement between metal oxides observed and metal oxides predicted by the thermodynamic stability diagrams are satisfactory, as can be seen in the SEM-photomicrographs and diagrams in Figures 10, 11 (a) and (b).

The thermodynamic stability of metal chlorides and oxides at a given temperature depends on the partial pressures of O and Cl. Since the corrosion tests performed in the present investigation were conducted under normal atmospheric condition, the oxides are the thermodynamically-stable phases.

Furthermore, in all cases the equilibrium gas composition falls within the field of stability of the oxides of these metals, see Figures 10, 11 (a) and (b). Thus, chlorides are not stable in contact with the gas phase but may possibly form in the scale at sites of sufficiently low  $P_{O_2}$ . Besides, at the metal-oxide interface the oxygen partial pressure is low and the chlorides become stable. Depending on the alloying elements, various volatile solid and gaseous chlorides can form at the interface, as given in Equation 3:



The process consisting of the formation of volatile metal chlorides (expressed in general terms by Equation 3), and subsequent oxidation of the evaporating chlorides is called 'active oxidation' [33], because no passivation occurs by a protective oxide layer but a very loose non-protective scale is formed. In this process chlorine is not consumed and thus plays mainly a catalytic role.

All these corrosion properties are desirable to be known for applications involving high-temperature processes like combustion and high-power operations. These two particular properties are evidently different to any specific condition which shows that the effect of surface layer on phase stability cannot be neglected.

For this research, we show that for the alloying elements added (Cr and Ti) to the master alloy (Fe40Al), many of these added elements display an usual temperature corrosion behavior as compared with other corroded alloys. This is determined by the equilibrium between the anodic and cathodic reactions occurring on the surface. The scope of corrosion reactions will be based upon parameters such as the available amount of time to complete the chemistry reaction, the number and condition of representative chemical alloyed elements, and the available electrolyte media to complete the anodic and cathodic reactions [34].

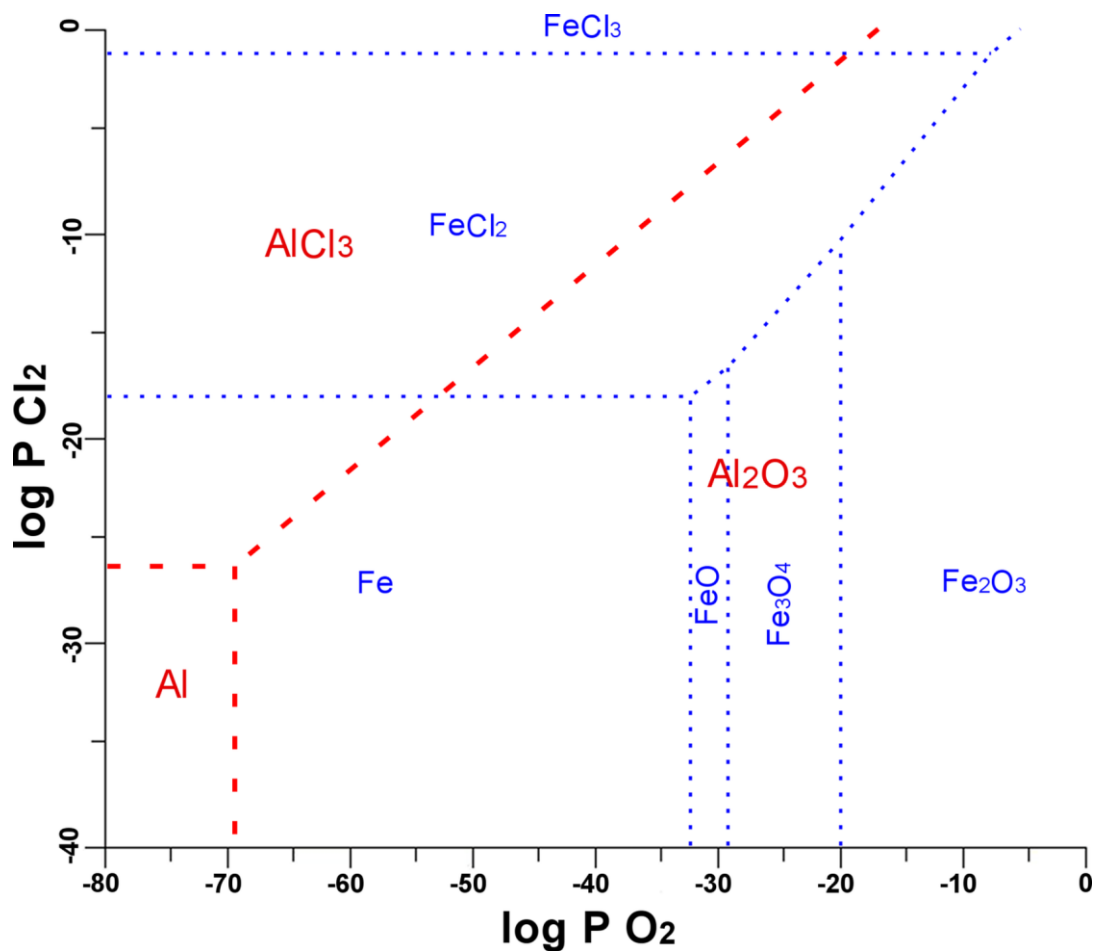


Figure 10. Thermodynamic stability diagrams for Fe-Al-Cl-O system at 450°C.

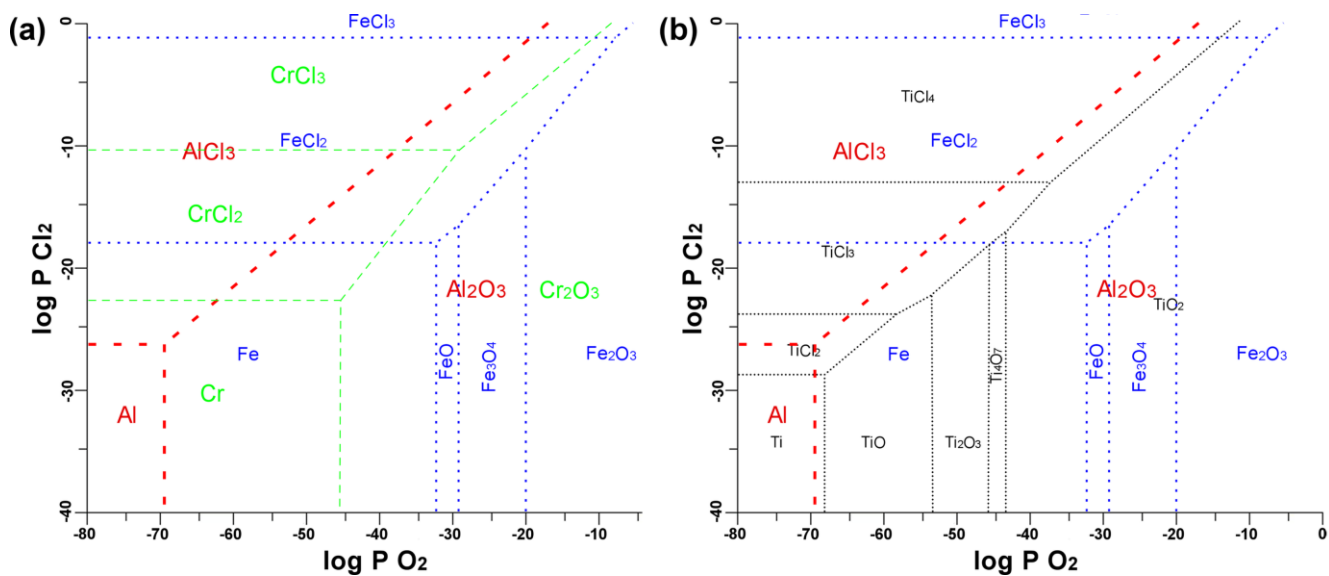


Figure 11. Thermodynamic stability diagrams for (a) Fe-Al-Cr-Cl-O at 450° C and (b) Fe-Al-Ti-Cl-O at 450°C.

## Fe-Al-Cr-Ti-Cl-O System

**Table 2.** Equilibrium constants for chemical reactions for the system Fe-Al-Cr-Ti-Cl-O at 450°C.

#	Reaction	Log K	#	Reaction	Log K
1	$4 \text{ Al(s)} + 3 \text{ O}_2 = 2 \text{ Al}_2\text{O}_3\text{(s)}$	209.297	16	$4 \text{ CrCl}_3 \text{(s)} + 3 \text{ O}_2 = 2 \text{ Cr}_2\text{O}_3\text{(s)} + 6 \text{ Cl}_2$	25.3498
2	$4 \text{ Cr(s)} + 3 \text{ O}_2 = 2 \text{ Cr}_2\text{O}_3\text{(s)}$	136.728	17	$2 \text{ TiCl}_2\text{(s)} + \text{Cl}_2 = 2 \text{ TiCl}_3\text{(s)}$	23.8658
3	$8 \text{ TiCl}_3\text{(s)} + 7 \text{ O}_2 = 2 \text{ Ti}_4\text{O}_7\text{(s)} + 12 \text{ Cl}_2$	100.35	18	$\text{Cr(s)} + \text{Cl}_2 = \text{CrCl}_2 \text{(s)}$	22.6421
4	$2 \text{ Al(s)} + 3 \text{ Cl}_2 = 2 \text{ AlCl}_3\text{(l)}$	79.0157	19	$4 \text{ Fe}_3\text{O}_4\text{(s)} + \text{O}_2 = 6 \text{ Fe}_2\text{O}_3\text{(s)}$	20.0696
5	$2 \text{ Ti(s)} + \text{O}_2 = 2 \text{ TiO(s)}$	68.2111	20	$4 \text{ FeCl}_2\text{(s)} + 3 \text{ O}_2 = 2 \text{ Fe}_2\text{O}_3\text{(s)} + 4 \text{ Cl}_2$	18.8497
6	$4 \text{ TiO(s)} + \text{O}_2 = 2 \text{ Ti}_2\text{O}_3\text{(s)}$	53.4893	21	$\text{Fe(s)} + \text{Cl}_2 = \text{FeCl}_2\text{(s)}$	18.0318
7	$4 \text{ AlCl}_3\text{(l)} + 3 \text{ O}_2 = 2 \text{ Al}_2\text{O}_3\text{(s)} + 6 \text{ Cl}_2$	51.2659	22	$4 \text{ FeCl}_3\text{(l)} + 3 \text{ O}_2 = 2 \text{ Fe}_2\text{O}_3\text{(s)} + 6 \text{ Cl}_2$	16.5278
8	$4 \text{ CrCl}_2 \text{(s)} + 3 \text{ O}_2 = 2 \text{ Cr}_2\text{O}_3\text{(s)} + 4 \text{ Cl}_2$	46.1594	23	$2 \text{ TiO(s)} + 3 \text{ Cl}_2 = 2 \text{ TiCl}_3\text{(s)} + \text{O}_2$	13.104
9	$4 \text{ Ti}_2\text{O}_3\text{(s)} + \text{O}_2 = 2 \text{ Ti}_4\text{O}_7\text{(s)}$	45.7872	24	$2 \text{ TiCl}_3\text{(s)} + \text{Cl}_2 = 2 \text{ TiCl}_4\text{(l)}$	12.943
10	$2 \text{ Ti}_4\text{O}_7\text{(s)} + \text{O}_2 = 8 \text{ TiO}_2\text{(s)}$	43.5057	25	$\text{TiCl}_4\text{(l)} + \text{O}_2 = \text{TiO}_2\text{(s)} + 2 \text{ Cl}_2$	11.5104
11	$2 \text{ TiCl}_3\text{(s)} + 2 \text{ O}_2 = 2 \text{ TiO}_2\text{(s)} + 3 \text{ Cl}_2$	35.9639	26	$2 \text{ TiCl}_2\text{(s)} + \text{O}_2 = 2 \text{ TiO(s)} + 2 \text{ Cl}_2$	10.7619
12	$2 \text{ Fe(s)} + \text{O}_2 = 2 \text{ FeO(s)}$	32.3568	27	$2 \text{ CrCl}_2 \text{(s)} + \text{Cl}_2 = 2 \text{ CrCl}_3 \text{(s)}$	10.4048
13	$6 \text{ FeO(s)} + \text{O}_2 = 2 \text{ Fe}_3\text{O}_4\text{(s)}$	29.3604	28	$3 \text{ FeCl}_2\text{(s)} + 2 \text{ O}_2 = \text{Fe}_3\text{O}_4\text{(s)} + 3 \text{ Cl}_2$	9.1198
14	$\text{Ti(s)} + \text{Cl}_2 = \text{TiCl}_2\text{(s)}$	28.7246	29	$2 \text{ FeO(s)} + 2 \text{ Cl}_2 = 2 \text{ FeCl}_2\text{(s)} + \text{O}_2$	3.7069
15	$4 \text{ TiCl}_3\text{(s)} + 3 \text{ O}_2 = 2 \text{ Ti}_2\text{O}_3\text{(s)} + 6 \text{ Cl}_2$	27.2814	30	$2 \text{ FeCl}_2\text{(s)} + \text{Cl}_2 = 2 \text{ FeCl}_3\text{(l)}$	1.161

## 4. CONCLUSIONS

A study of the effect of 2.5 at. % Cr and Ti on the corrosion behavior of Fe40Al in molten KCl-ZnCl<sub>2</sub> (1:1M) at 450°C was performed using electrochemical techniques. Polarization curves showed that by adding Cr, the alloy was passivated. The highest corrosion rate was obtained by adding 2.5 at.% Cr, whereas the lowest corrosion rate corresponded to the Fe40Al binary alloy. EIS data demonstrated that the corrosion rate was controlled by the formation of an external corrosion products external film, which was dissolved by the Cl-containing molten salt.

Addition of Ti induced a better corrosion performance than Fe40Al2.5Cr alloy, this behavior was due to the formation of a non-porous aluminum oxide layer modified with titanium oxide. The stability of this external film provided the corrosion resistance of the alloy.

FeAl-based alloys studied in this work showed a greater resistance to corrosion than Ni alloys (Ni-20Cr wt.%) and 304 SS steel under the same test conditions of corrosion. These last two materials are currently considered as candidate alloys for high-temperature processes such as combustion and high-power operations.

We conclude that these FeAl-base alloys show great promise for applications involving high-temperature processes like combustion and high-power operations with their superior corrosion resistance, which may provide a longer and more stable product life for incinerator heat exchanger linings.

#### ACKNOWLEDGEMENT

The authors express their gratitude to CONACyT for the financial support granted for the development of this research.

#### References

1. J Winkler, *International Journal of Life Cycle Assessment*, 10 2 (2005) 156.
2. R. Changkook, *Journal Of The Air & Waste Management Association (Air & Waste Management Association)*, 60 2 (2010) 176.
3. B.Q. Wang, *Wear*, 188 (1995) 40.
4. Y. L. Nava, Y. S. Zhang, M. Takemoto and R. A. Rapp, *Corros. Sci.*, 52 (1996) 680.
5. Y.S. Li., Y. Niu and W.T. Wu, *Mater. Sci. Eng. A*, 345 (2003) 64.
6. M.A. Uusitlao, P.M.J. Vuoristo and T.A. Mäntylä, *Mater. Sci. Eng. A*, 346 (2003) 168.
7. G.Y. Lai and G. Sorell, *Materials Performance in Waste Incineration Systems*, NACE International, (1992).
8. J. L. He, C.H. Yu, A. Leyland, A.D. Wilson, A. Matthews, *Surf. Coat. Technol.*, 155 (2002) 67.
9. C. Houngninou, S. Chevalier, J. P. Larpin, *Appl. Surf. Sci.*, 236 (2004) 256.
10. S.W. Banovic, J.N. Dupont and A.R. Marder, *Mater. High Temp.*, 16 (1999) 195.
11. [P. Elliott, A.A. Ansari, R. Prescott and M.F. Rothman, *Corros. Sci.*, 44 (1988) 544.
12. C. Schwal and M. Scheutze, *Mater. Corros.*, 51 (2000) 161.
13. Y.S. Li, Y. Niu and W.T. Wu, in: 12th Asian-Pacific Corrosion Control Conference, Seoul, 2001. 847.
14. R. A. Rodríguez-Díaz, J. Uruchurtu-Chavarín, A. Molina-Ocampo, J. Porcayo-Calderón, M. González-Pérez, J.M. López-Oglesby, J. G. Gonzalez-Rodríguez and J. A. Juárez-Islas, *Int. J. Electrochem. Sci.*, 8 (2013) 958.
15. C. A. C. Sequeira and M. G. Hocking, *Journal of applied electrochemistry*, 8 2 (1978) 145.
16. M.A. Espinosa-Medina, M. Casales, A. Martinez-Villafañe, J. Porcayo-Calderon, L. Martinez, J.G. Gonzalez-Rodriguez, *Materials Science and Engineering. A*, 300 1–2 (2001) 183.
17. T. J. Pan, W. M. Lu, Y. J. Ren, W. T. Wu and C. L. Zeng, *Chemistry and materials science, oxidation of metals*, 72 3-4 (2009), 179.
18. C. L. Zeng, W. Wang and W. T. Wu, *Chemistry and materials science, oxidation of metals*, 53 3-4 (2000) 289.
19. C. L. Zeng, W. Wang, and W. T. Wu, *Corrosion Science*, 43 4 (2001) 787–801.
20. T.B. Massalski, *Binary alloy phase diagrams*, 1 (1986) 112.
21. D. Li, d. Lin and Y. Liu, *Mat. Sci. and Eng. A*, 249 (1998) 206.
22. M. Palm, G. Inden and N. Thomas, *Journal of phase equilibria*, 16 3 (1995), 209.
23. A. Argawal, R. Balasubramaniamn, *Practical metallography*, 33 (1996), 453.
24. A. Agarwal, M. J. Akthar, R. Balasubramaniamn, *J. Mat. Sci.*, 31 (1996) 5207.
25. J. Porcayo-Calderon, O. Sotelo-Mazón, V.M. Salinas-Bravo, C.D. Arrieta-Gonzalez, J.J. Ramos-Hernandez and C. Cuevas-Arteaga, *Int. J. Electrochem. Sci.*, 7 (2012) 1134.
26. M. J. O'Neil, *The Merck Index: An Encyclopedia of Chemicals, Drugs, and Biologicals*, 14th Edition, Merck, New Jersey (2006).

27. P.L. Daniel, R.A. Rapp, *Adv. Corros. Tech.*, 5 (1976) 55.
28. D. Li, Y. Xu, D. Lin, *J. Mater. Sci.*, 36 (2001) 979 – 983
29. Y.S. Li, M. Al-Omary, Y. Niu, K. Zhang, *High Temp. Mater. Proc.*, 21 (2002) 12.
30. Y. Shinata, F. Takahashi, K. Hashiura, *Mater. Sci. Eng. A*, 87 (1987) 399.
31. Y.S. Li, M. Sanchez-Pasten, M. Spiegel, *Mater. Sci. Forum*, 461–464 (2004) 1047.
32. A. Ruh, M. Spiegel, *Corros. Sci.*, 48 (2006) 679.
33. M.J. McNallan, W.W. Liang, S.H. Kim, C.T. Kang, in: R.A. Rapp (Ed.), *High Temperature Corrosion*, NACE International, Houston Texas (1983) 316-321.
34. D. Batau, A. Georgeta Cosmeleata, A. Aloman, *Sci. Bull*, 68(4) (2006) 77.